

High Energy Laser Testbed for Accurate Beam Pointing Control

Dojong Kim^a, Jae Jun Kim^{*b}, Duane Frist^b, Masaki Nagashima^b, Brij Agrawal^b
^aAgency for Defense Development, Daejeon, Republic of Korea;
^bNaval Postgraduate School, Monterey, CA USA 93943

ABSTRACT

Precision laser beam pointing is a key technology in High Energy Laser systems. In this paper, a laboratory High Energy Laser testbed developed at the Naval Postgraduate School is introduced. System identification is performed and a mathematical model is constructed to estimate system performance. New beam pointing control algorithms are designed based on this mathematical model. It is shown in both computer simulation and experiment that the adaptive filter algorithm can improve the pointing performance of the system.

Keywords: HEL, Jitter Control, Beam Control, Adaptive Filter

1. INTRODUCTION

High Energy Laser (HEL) systems are ready for some of the most challenging military applications in future battle fields since speed of light delivery enables the war fighter to engage very distant targets immediately. Technology issues on HEL systems include various types of high energy laser devices, beam control systems, atmospheric propagation, and target lethality issues. Among them, precision pointing of laser beam and high-bandwidth rejection of jitter produced by platform vibrations are the key technologies in the emerging fields of laser communications and HEL systems.

Optical beam control describes the centroid shifting of a laser on the target and is a concern of engineers and scientists working with lasers and electro optical systems. Platform motion and optical component motion causes optical jitter, resulting in poor pointing accuracy and blurred images. Even a small level relative motion between mirrors and lenses can degrade the performance of precision pointing systems. Sources contributing to optical jitter include thermal effects, mechanical vibration, acoustics, static and dynamic loading, and heating and cooling systems.

The HEL testbed has been developed at the Naval Postgraduate School to support the research environments on the precision beam control technology including acquisition, tracking, and pointing. The testbed incorporates optical table, two axis gimbal, high speed computers, and a variety of servo components, sensors, optical components, and software. System configuration, system identification, and mathematical model of the HEL testbed are presented. Based on these results, beam pointing control algorithms including adaptive filters are designed. Computer simulation and experimental results are presented to show that the new control algorithm can improve the pointing performance of the system.

2. HIGH ENERGY LASER BEAM CONTROL TESTBED

2.1 Configuration of HEL Beam Control Testbed

The objective of the HEL testbed is to provide a research environment for the development of new technologies related with acquisition, tracking, pointing, and optical beam control of maritime HEL systems. The actual testbed uses a low power laser to maintain a safe laboratory environment. The testbed is built by Boeing-SVS, and the picture of the testbed is shown in Figure 1. The HEL testbed consists of three major components; host computer, target computer, and beam control system. A simple architecture of the testbed and control block diagram are shown in Figures 2.

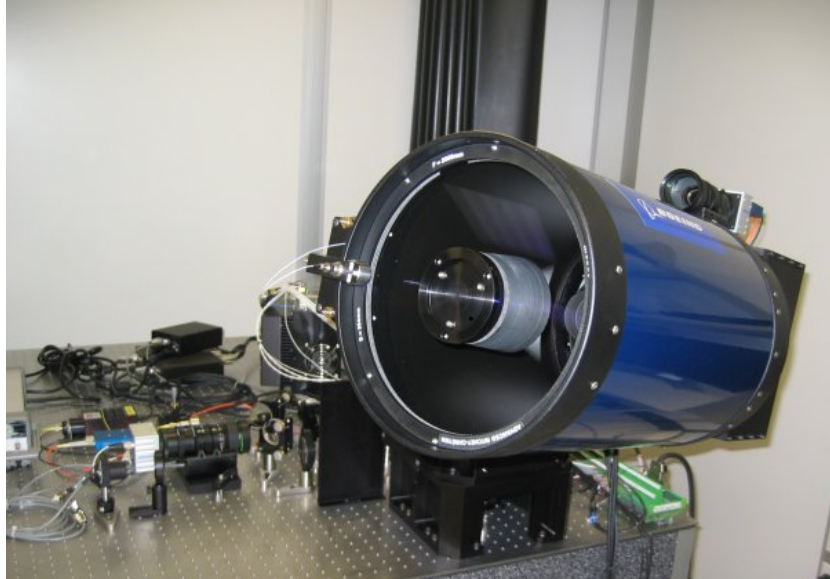


Figure 1. NPS HEL Beam Control Testbed with 10 inch Telescope

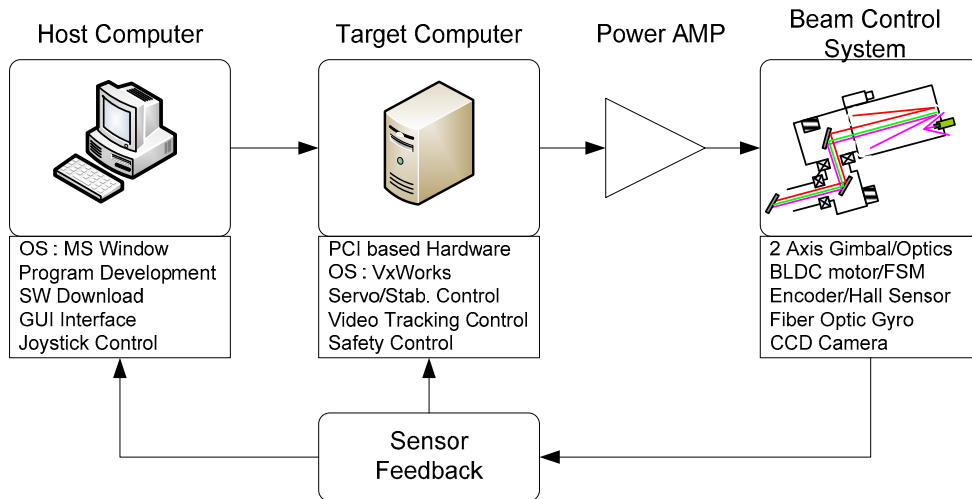


Figure 2. System Configuration

The host computer is a MS Windows based personal computer in which all the software is developed, compiled, debugged, and tested. Final object codes are downloaded to the target computer via Ethernet connection. A two axis joystick is attached to the host computer and generates motion commands. System operation mode is controlled by switches on the joystick. Graphical user interfaces are also implemented to support various operational modes.

The Target computer is a VxWorks supported CompactPCI based system and consists of four 3U size boards: PowerPC compactPCI processor board (IMP2A), IO Pack Carrier board (ACPC8630), Multifunction CompactPCI board (ACPC730), and Counter Timer board (ACPC484). The PowerPC board mainly executes real time code at 1 kHz and controls all the subsystems. A frame grabber PMC card is also mounted on the board to control and communicate with the video tracking cameras which are connected by camera link. The PowerPC board communicates with the Host computer by Ethernet from which it downloads software, and receives the control commands and uploads the system status to the Host computer. An IO Pack carrier board has a PMC module which is connected to gyros by synchronous interface to control and receive angular rate data. The multifunction board is a precision CompactPCI board with the

capability to monitor analog input signals. In addition, eight 16-bit analog voltage output channels and 16 digital input/output channels are provided and are connected to motor control command, FSM control command, and various discrete signals. Lastly, rotary encoders providing relative positions are connected to the Counter Timer board. The External Interface Diagram of the target computer is presented in Figure 3.

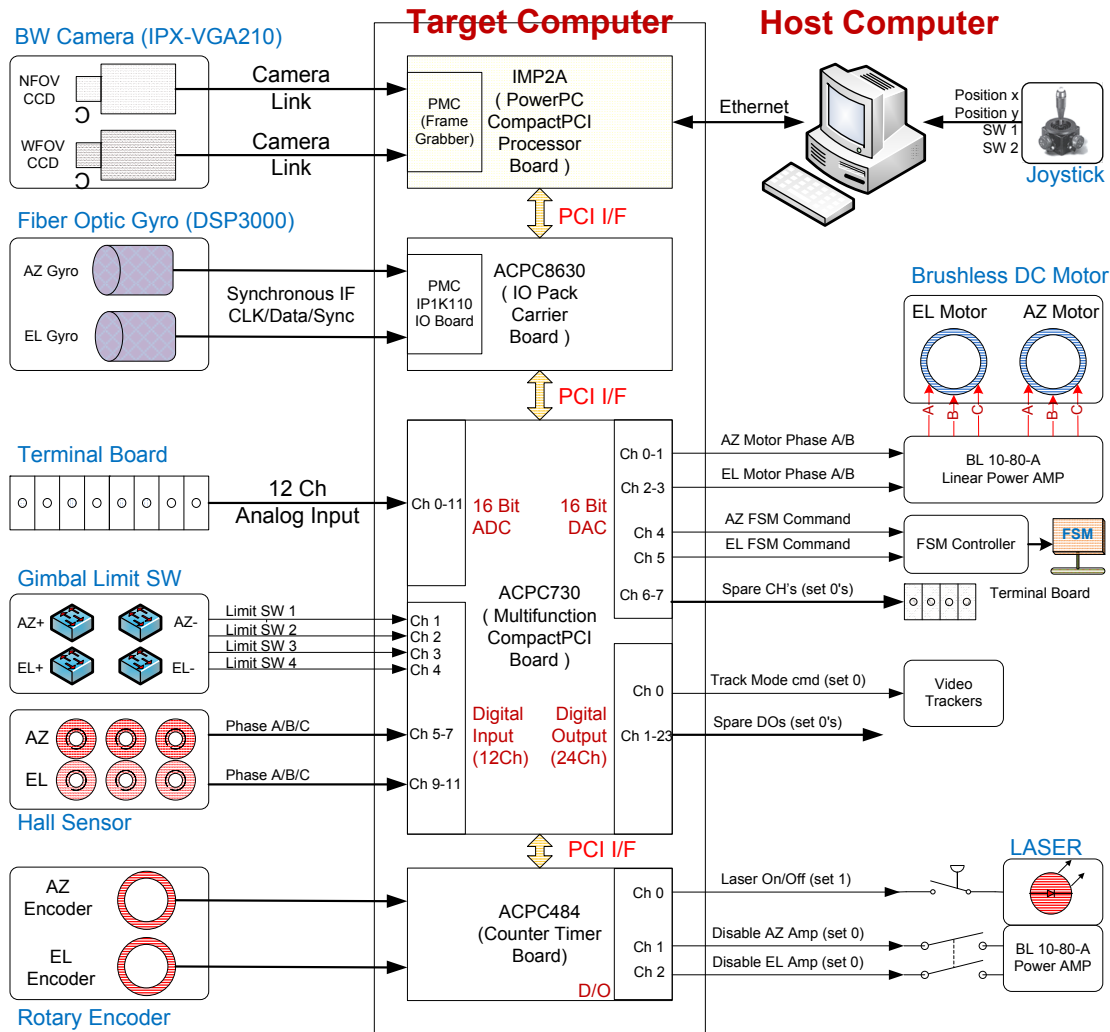


Figure 3. External Interface Diagram of the Target Computer

The major components of the beam control system consists of Wide Field-of-View (WFOV) video tracking system, Narrow Field-of-View (NFOV) video tracking system, alignment and beam jitter control system, supporting optics, and laser sources. The schematic of the beam control system is shown in Figure 4. The WFOV video tracking system consists of a WFOV camera, two rate gyros, two rotational stages, and supporting hardware. The WFOV control system is designed to stabilize the azimuth and elevation of the telescope gimbals and maintain the line of sight (LOS) to the target in the inertial space with respect to external disturbances.

The NFOV video tracking system consists of a NFOV camera and a Fast Steering Mirror (FSM). The NFOV control system maintains fine tracking and pointing of a laser beam on a target.

The alignment and beam jitter control system consists of a reference laser, a beam Position Sensing Device (PSD), and a FSM. The reference laser at the end of the telescope travels through the telescope and the optical path to reach PSD. The FSM is used to correct any misalignment and relative jitter.

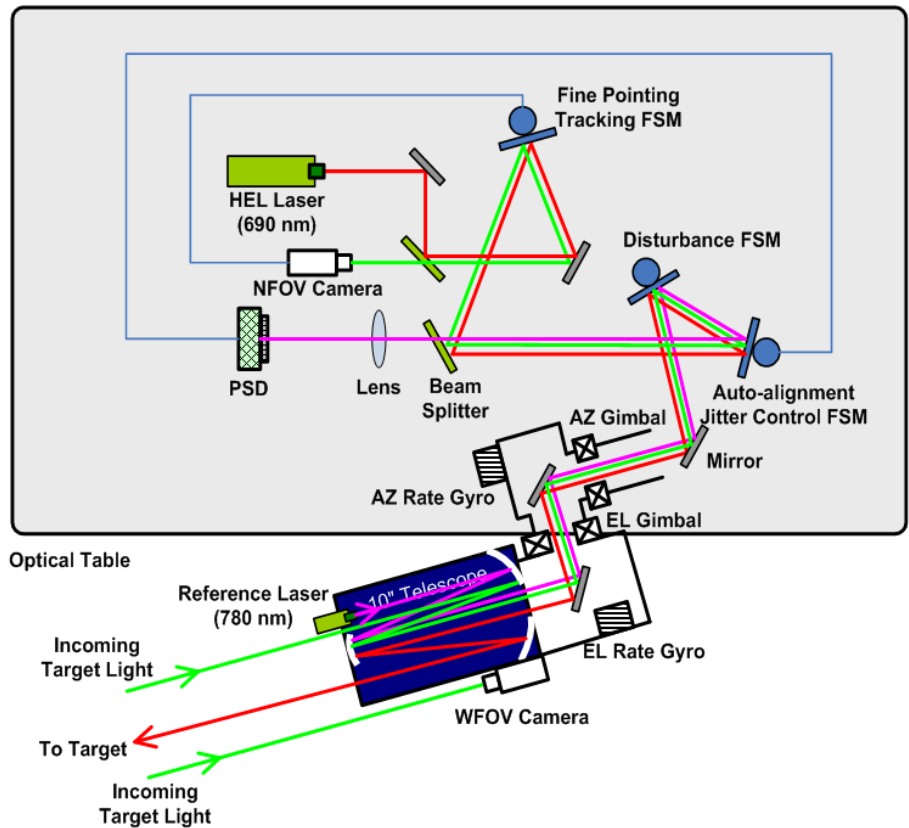


Figure 4. Schematic of the Beam Control System

2.2 Control System Design

2.2.1 Wide Field-of-View (WFOV) Video Tracker Control

The WFOV control system consists of an inner loop and outer loop as shown in Figure 39. The inner loop is a rate control loop, which provides stabilization with respect to external disturbances and tracking functions based on gyro feedback. The outer loop is an angular control loop that automatically maintains LOS to the target center based on WFOV camera feedback. The inner rate loop has a PI controller and structural notch filters. A PI controller is also implemented on the outer loop.

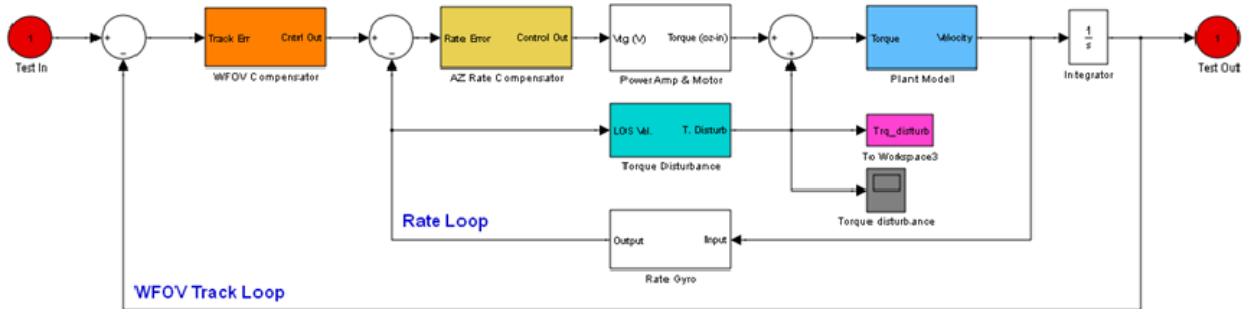


Figure 5. WFOV Control Loop

2.2.2 Narrow Field-of-View (NFOV) Video Tracker Control Loop

The NFOV control loop shown in Figure 6 includes an integrator type compensator (on each axis).

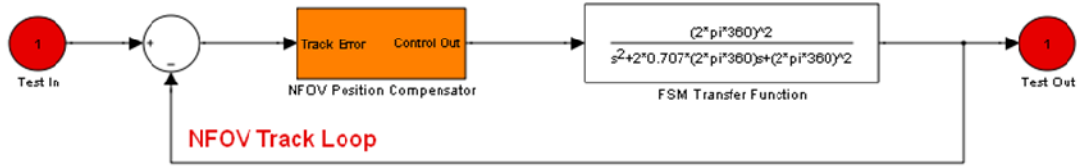


Figure 6. NFOV Control Loop

2.2.3 Alignment and Beam Jitter Control

The auto-alignment/jitter control FSM is controlled using an analog controller with an adjustable gain. The PSD signal is used as a feedback signal to the analog controller.

2.3 System Identification

Several types of experiments were performed to determine characteristics of the HEL testbed. The results of the tests were utilized for system modeling. The experiments include resonant frequency test, rate loop servo bandwidth and stabilization test, FSM test, and NFOV bandwidth test. The target computer has an external terminal board which interfaces all the signals between the beam control system and target computer. It also provides input/output test points. Test equipment such as a dynamic signal analyzer, data acquisition system, and oscilloscope are used for signal generation, data storage, and observation of test signals.

2.3.1 WFOV Resonance Frequency

Random signals were applied to the power amplifier of the azimuth and elevation gimbal stages and output signals were received at the gyro and encoder respectively. With this open loop tests, resonance frequencies were calculated using power spectral density analysis. Prior to performing the analysis, preprocessing was required to remove constant drift in addition to outliers. The resonance frequencies are determined over a frequency range of 0-200Hz.

Table 1 – Summary of Resonance Frequency Test

Direction	Output signal	Resonance frequencies (Hz)
AZ	Gyro	2.6, 8.3, 11.4, 15.9, 36.6, 69.5, 101, 134, 147.7
	Encoder	2.6, 8.2, 11.4, 101
EL	Gyro	3.8, 10, 14.9, 43.3, 61.4, 74.5, 101, 145, 195
	Encoder	3.8, 11.6, 61.4, 101

2.3.2 WFOV Rate Loop Serve Bandwidth

Rate loop bandwidth was measured by applying a sweep sine signal to rate command and observing output at the gimbal gyro. As with resonance testing, preprocessing was conducted for trend removal and outlier rejection. Data was measured from 1-50Hz for both axis. The ultimate goal of this testing is to determine the transfer function of the rate loop servos. Several intermediate calculations were required to make this determination, the first of which is the cross-correlation sequence as given by

$$R_{xy}(m) = E\{x_{n+m} \cdot y_n^*\} = E\{x_n \cdot y_{n-m}^*\} \quad (1)$$

where x_n and y_n are jointly stationary random processes, and $E\{\cdot\}$ is the expected value operator. In reality, a correlation estimate given by Equation 2 have to be used since only a finite segment of one realization of the infinite length random process was available.

$$\hat{R}_{xy}(m) = \begin{cases} \sum_{n=0}^{N-m-1} x_{n+m} \cdot y_n^* & m \geq 0 \\ \hat{R}_{yx}^*(-m) & m < 0 \end{cases} \quad (2)$$

Additionally, coherence function calculation was also required. Coherence shows the portion of the output spectrum related to the input spectrum as given by Equations (12)-(14)

$$\gamma^2 = \frac{G_{xy} \cdot G_{xy}^*}{G_{xx} \cdot G_{yy}} \quad (3)$$

$$G_{xy} = FFT(\hat{R}_{xy}) \quad (4)$$

$$G_{xx} = FFT(\hat{R}_{xx}) \quad (5)$$

where G_{xy} is the cross spectrum and G_{xy}^* is its complex conjugate, G_{xx} is the input power spectrum and the output power spectrum.

Coherence is an indication of statistical validity of frequency response measurements and is measured on a scale of 0.0-1.0, with a value of 1.0 corresponding to perfect coherence. Reasons for a coherence value less than one include poor resolution, nonlinearities, extraneous noise and uncorrelated input signals. Additionally, it is independent of the shape of the frequency response function since it has been normalized. Finally, the frequency response, also called the “Transfer function” is calculated based on a ratio of the cross spectrum to input power spectrum as given by

$$H(f) = \frac{G_{xy}}{G_{xx}} \quad (6)$$

The resulting transfer functions are shown in Figures 7 and 8. The 3dB bandwidth is 6Hz for the azimuth axis, and 7Hz for elevation. Additionally, resonance frequencies in the azimuth axis of 8.2Hz, 11.4Hz, and 15.9Hz caused significant reduction in tracking performance.

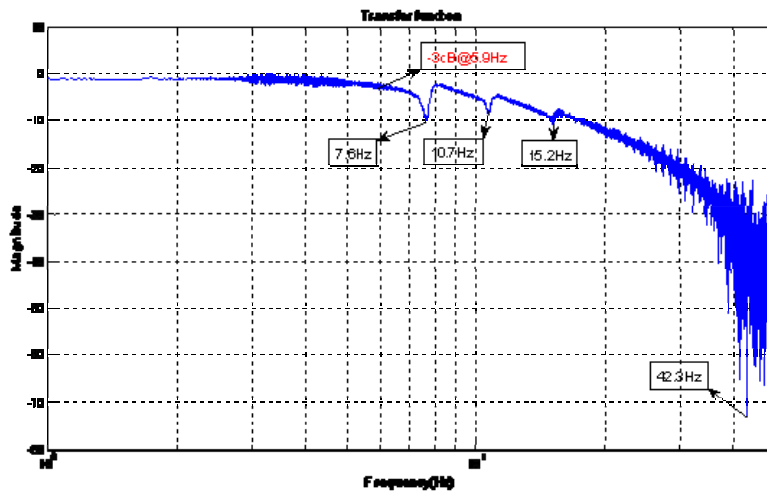


Figure 7. Azimuth Axis Transfer Function

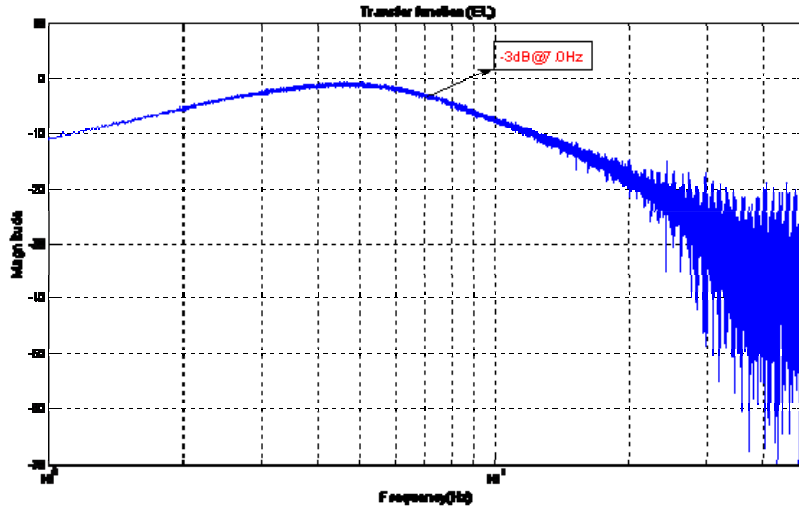


Figure 8. Elevation Axis Transfer Function

2.3.3 WFOV Rate Loop Stabilization

By applying a disturbance to the input of the power amplifier and measuring torque error, one is able to determine the torque rejection characteristics. A sweep sine signal over the frequency range of 1-100Hz is applied. Error output in frequency domain is shown in Figures 9 and 10. Test results show the torque rejection ration is low over the tested frequency range. Additionally, stabilization and servo tracking performance were adversely affected by resonance frequencies.

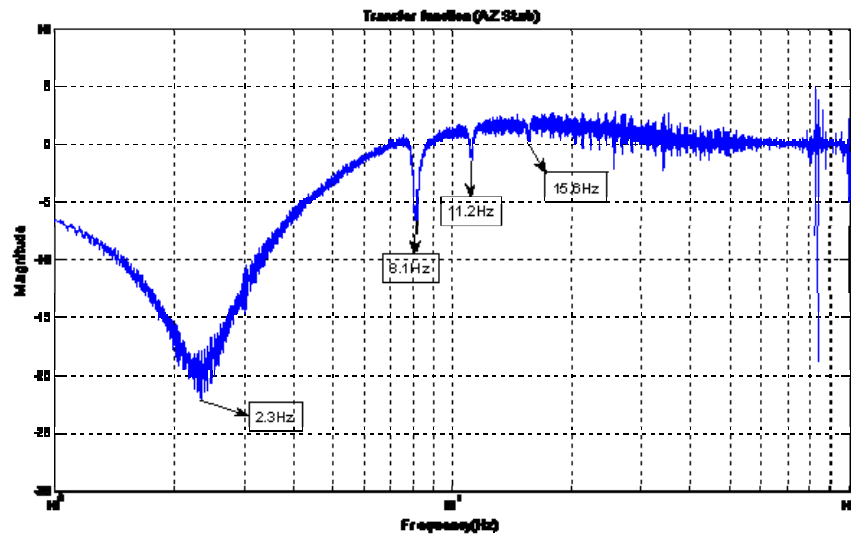


Figure 9. Azimuth Rate Stabilization Transfer Function

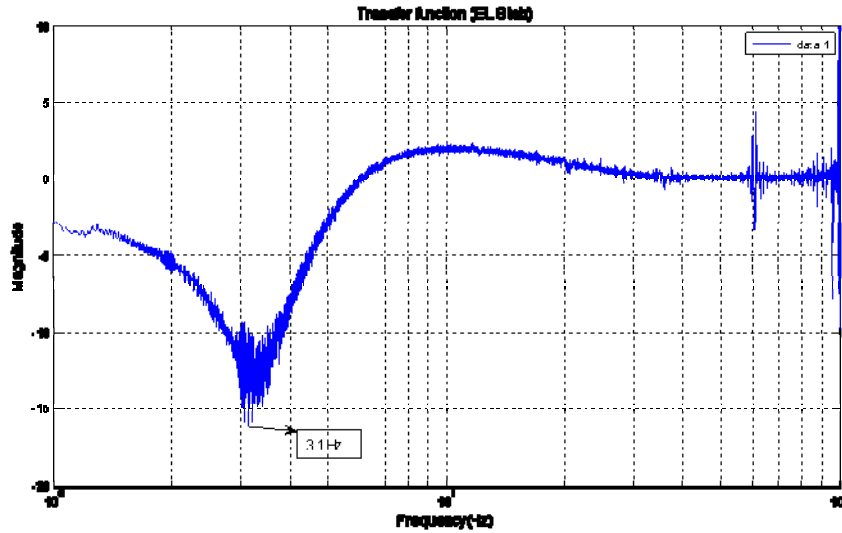


Figure 10. Elevation Rate Stabilization Transfer Function

2.3.4 Fast Steering Mirror

FSMs have been used for a number of years for target acquisition, scanning and beam steering. A push/pull configured voice coil drives a two axis mirror. This setup is similar to a speaker coil, with the difference being the FSM is configured with a moving magnet versus a moving coil as is the case for a speaker. The mirror is flexurally suspended and includes an optical sensor as well as a local feedback system. Local position feedback is the inner loop of the NFOV control loop. FSM dynamic characteristics were determined by applying a sweep sine signal to the local position input command and taking output from the position sensor, see Figure 32. Frequency range for the test was 1-1000Hz with an input voltage of 0.5Vpk. Tests were conducted on both azimuth and elevation axis. Results from frequency response tests are shown in Figures 33 and 34. As one would expect, the transfer function in nearly identical between the two axis, and both have a -3dB bandwidth of 360Hz.

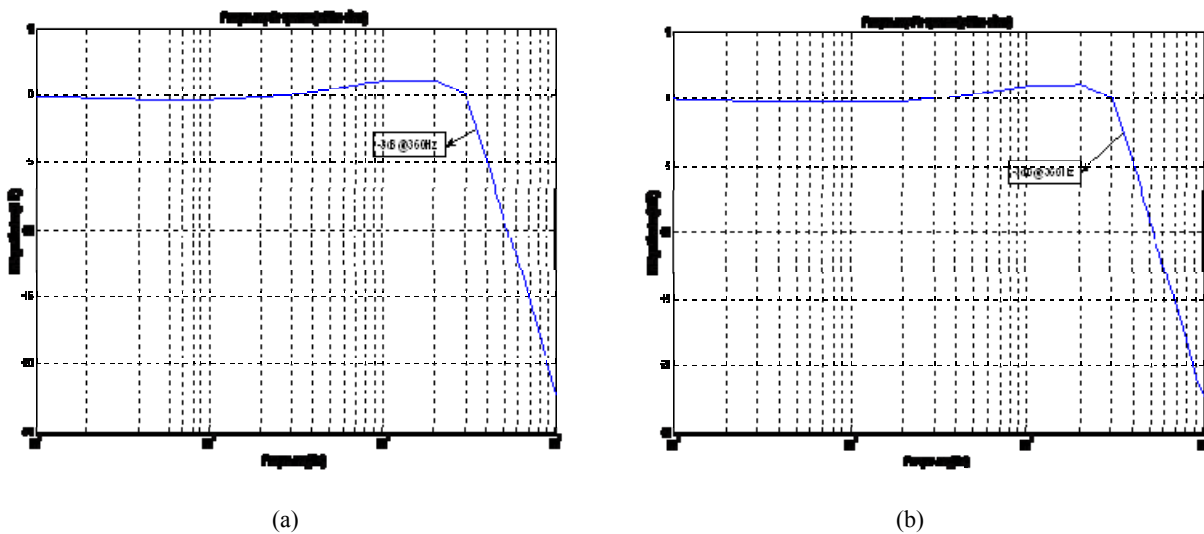


Figure 11. FSM Transfer Function: (a) Azimuth, (b) Elevation

2.3.5 NFOV Control Bandwidth

A sweep sine signal is applied to the position input of the first FSM and the output signal is measured as the position output of the second FSM as shown in Figure 12. The transfer function for each axis was nearly identical regardless of input magnitude. In both axis, the -3dB bandwidth was 13Hz as shown in Figure 13.

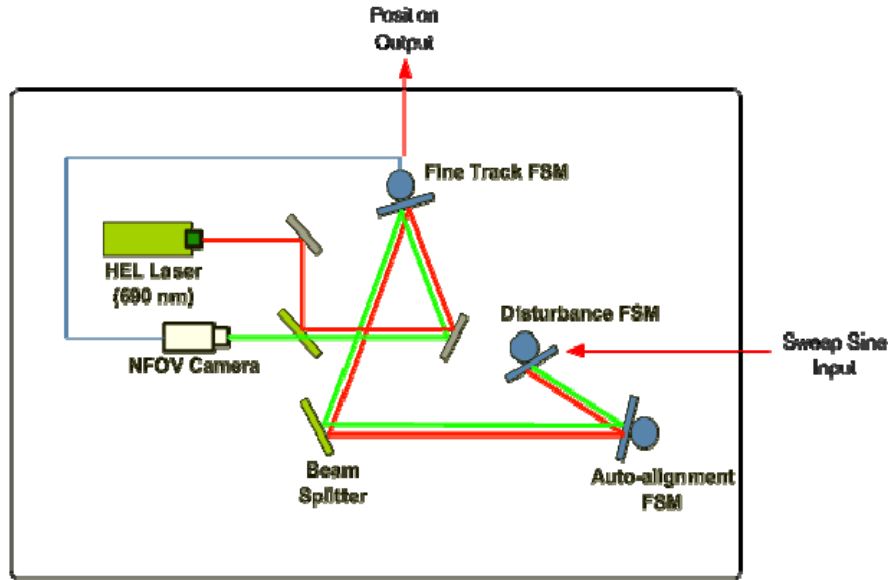


Figure 12. Test setup for NFOV track loop

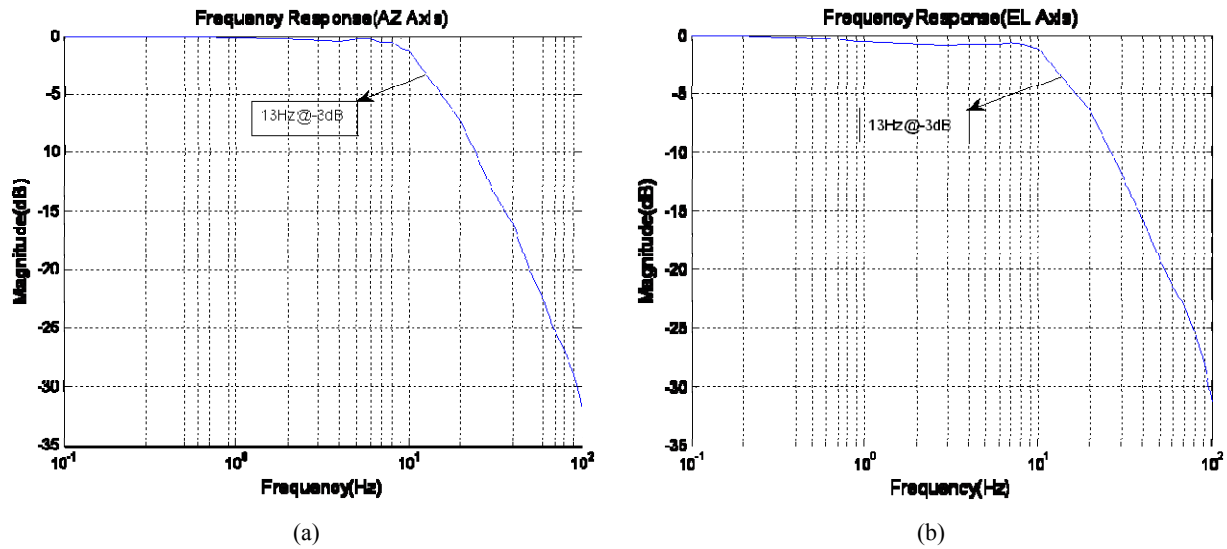


Figure 13. NFOV video tracker transfer function: (a) azimuth, (b) elevation

2.3.6 Alignment and Beam Jitter Control

Since the alignment and beam jitter control loop uses an analog sensor (PSD) and an analog controller, we expect that the control bandwidth is higher than the NFOV tracker. However, the actual testing was not performed.

For adaptive filters, the reference input needs to be coherent with the disturbance sources. Like classical time invariant control systems, adaptive filtering techniques can be applied using feedforward or feedback. For a feedforward system, the reference input is determined by measuring the disturbance. For feedback adaptive filters, the reference input is an estimation of disturbance from your system error. Typically, the filter output passes through the secondary plant (for example corrective element such as FSM) prior to its effects being measured at the target sensor. The secondary plant will cause phase and gain variation. By placing a copy of the secondary plant transfer function in the reference signal path to the weight updating algorithm, such variations can be avoided. This is Filtered-X method [4]. At each time step, the weights must be updated to reduce the system error. There are two primary methods for updating weights, least-mean-square (LMS) and recursive-least-square (RLS).

3.1.1 Recursive Least Mean Squares (LMS) Method

The adaptive filter in Figure 15 can be written as

$$y(n) = \mathbf{w}^T(n)\mathbf{r}(n) \quad (8)$$

where $\mathbf{w}(n) = [w_0(n), w_1(n), w_2(n), \dots, w_M(n)]^T$ and $\mathbf{r}(n) = [r(n), r(n-1), \dots, r(n-M+1), r(n-M)]^T$. An easy way to quantify the system error is using the mean square of the error signal, $\xi = E\{e^2(n)\}$ [2]. The LMS method uses a gradient of the error to determine the steepest descent for minimizing ξ . The upgraded weights are computed by the following equation:

$$\mathbf{w}(n+1) = \mathbf{w}(n) + \mu\mathbf{r}(n)e(n) \quad (9)$$

3.1.2 Recursive Least Mean Squares (RLS) Method

Another method of updating the weighting vector is the use of recursive-least-squares (RLS), which provides faster convergence and lower steady state errors than LMS. The RLS algorithm contains a cost function, which maintains a memory of errors according to a forgetting factor of $0 < \lambda \leq 1$. Where LMS method attempts to minimize the mean square of the current error, the RLS algorithm minimizes a summation of the square of all errors multiplied by the forgetting factor, λ [4]:

$$E(n) = \sum_{i=1}^n \lambda^{n-i} e^2(i) \quad (10)$$

The purpose of the forgetting factor is to more heavily weight recent data so that nonstationary disturbances can be accounted for. Equations (11), (12), and (13) summarize the FX-RLS algorithm for updating the weighting vector $\mathbf{w}(n)$ at each time step [4],[6].

$$\mathbf{w}(n) = \mathbf{w}(n-1) + \mathbf{k}^T(n)e(n) \quad (11)$$

$$\mathbf{k}(n) = \frac{\lambda^{-1}\mathbf{Q}(n-1)\hat{\mathbf{r}}(n)}{1 + \lambda^{-1}\hat{\mathbf{r}}^T(n)\mathbf{Q}(n-1)\hat{\mathbf{r}}(n)} \quad (12)$$

$$\mathbf{Q}(n) = \lambda^{-1}\mathbf{Q}(n-1) - \lambda^{-1}\mathbf{k}(n)\hat{\mathbf{r}}^T(n)\mathbf{Q}(n-1) \quad (13)$$

Another advantage of the RLS methods is that the weighting values will approach those of the optimal Wiener filter weightings, which is not the case for LMS [4].

3.2 Narrow Field-of-View (NFOV) Video Tracker Control with Adaptive Filters

Adaptive control was implemented on the NFOV using the video tracker error. This implementation is of the feedback type by estimating the disturbance from a video tracker error signal. The adaptive controller is added in series with the proportional-plus-integral (PI) controller. Additionally, both Filtered-X(FX)-LMS and Filtered-X(FX)-RLS adaptive

algorithms are implemented in the computer simulation. NFOV video tracker simulations were conducted with three disturbance sources. The first two were from mechanical vibration, one at 20 Hz and another at 50 Hz. The third disturbance was a 0.5 Hz sinusoidal in addition to broadband white noise. This was to simulate the effects of a target motion. Only the PI controller was active for the first two seconds of all simulations. A comparison of FX-LMS and FX-RLS performance is shown in Figures 16 through 17. The frequency analysis shown in Figures 16 and 17 was conducted on the steady state period of 9-12 seconds. As expected, there is a significant reduction in target pointing error once the adaptive filter is engaged. Both LMS and RLS algorithms reduced RMS target error to less than one quarter of that produced by the PI controller alone. While the FX-RLS algorithm produces lower steady state error, it has the drawback of significant transient errors. The FX-LMS algorithm is much slower to converge as demonstrated by the significant error spike seen through ten seconds of simulation. Further indication that FX-LMS is slower to converge can be seen in Figure 18, which illustrates the convergence of FX-LMS and FX-RLS weights. After ten seconds, FX-RLS weights have stabilized, while FX-LMS weights continue to change.

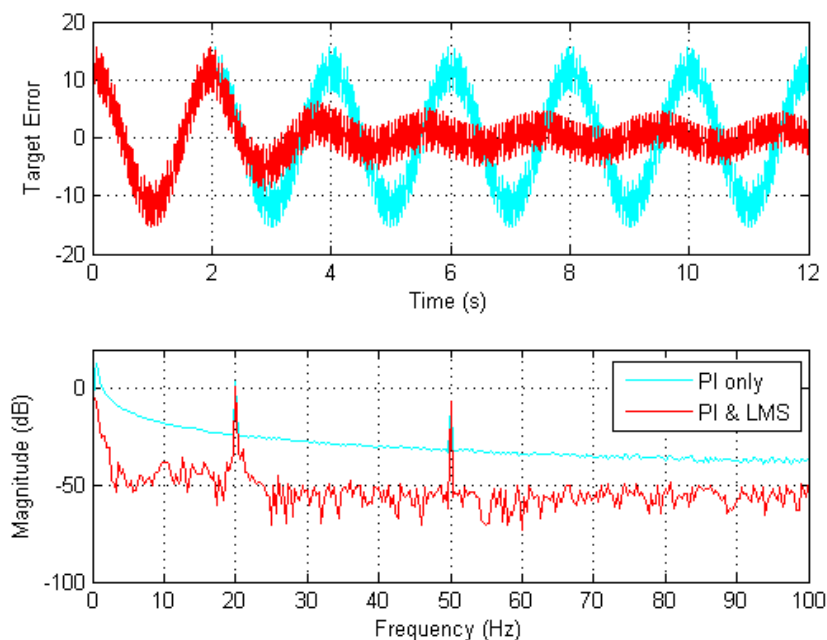


Figure 16. Target error using NFOV FX-LMS controller

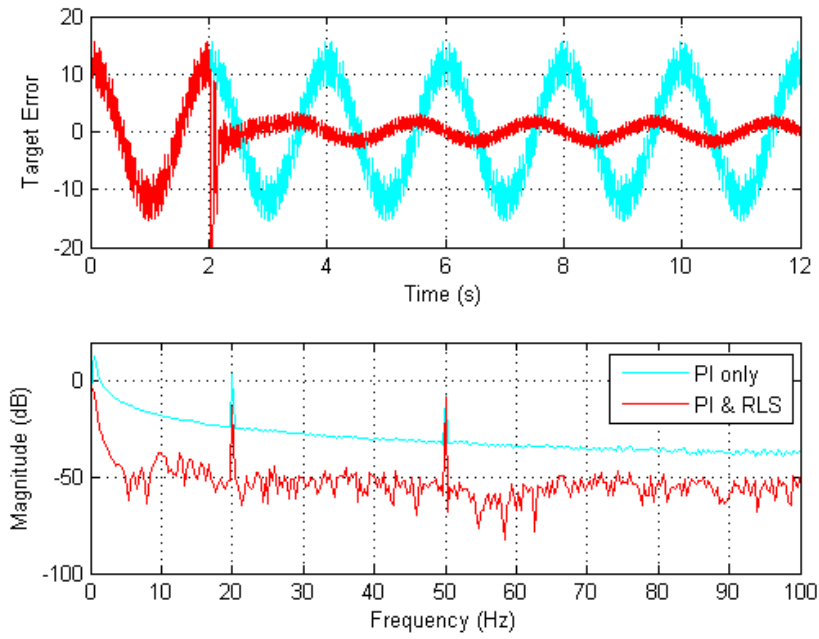


Figure 17. Target error using NFOV FX-RLS controller

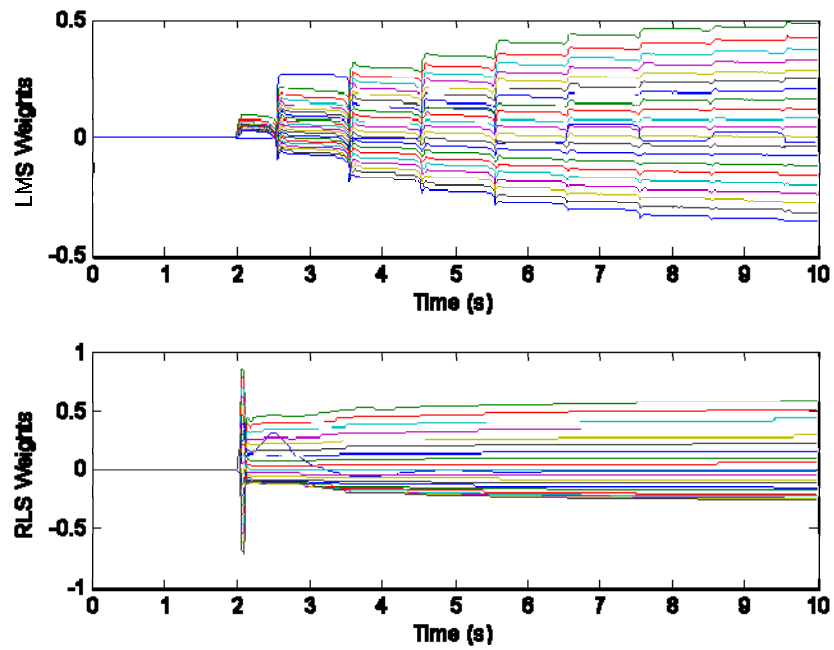


Figure 18. NFOV Video tracking adaptive filter weights comparison

3.3 Beam Jitter Control

The HEL beam control testbed uses a reference laser for optical beam alignment and jitter control. Since the PSD will only measure the relative jitter between the reference laser and the PSD, the beam jitter will not be completely corrected with the initial control design. Typically, Inertial Reference Unit (IRU) with an inertially stable reference laser is employed in the system to overcome this problem. However, implementation of IRU in the system will increase the system cost and complexity. In order to minimize the complexity of the system, a strap-down IRU implementation is considered with additional rate gyro sensors on the reference laser.

Two parallel adaptive filters are designed for the strap-down IRU system - the feedforward adaptive filter using the rate gyro sensors, and the feedback adaptive filter using the PSD. While the NFOV tracker also can detect some of the disturbance vibration (sees it as target motion), on-board rate gyros and PSDs are typically more accurate and have higher bandwidth than the video tracking system for platform disturbance. The feedforward adaptive controller was implemented using FX-RLS only, while the feedback adaptive controller was implemented using both FX-LMS and FX-RLS. The feedforward adaptive controller uses the gyro signal as a reference and estimates the error by subtracting the filtered output from the reference signal. The feedback adaptive controller is similar to the video tracking adaptive filter, since both estimate the disturbance based on the error and filter output. The filter command calculated by both IRU controllers is summed and sent to the auto-alignment FSM.

Simulations were conducted using the same 0.5 Hz, 20 Hz, and 50 Hz sinusoidal signals along with broadband white noise. Simulation results can be seen in Figures 19 and 20. For both plots, the IRU adaptive filters are active after 4 seconds. The frequency analysis is from the steady state period of 9-12 seconds. Using the adaptive feedback controller combined with the feedforward adaptive controller using the gyros results in an RMS error of 4.6 for the LMS algorithm and 4.0 for the RLS algorithm.

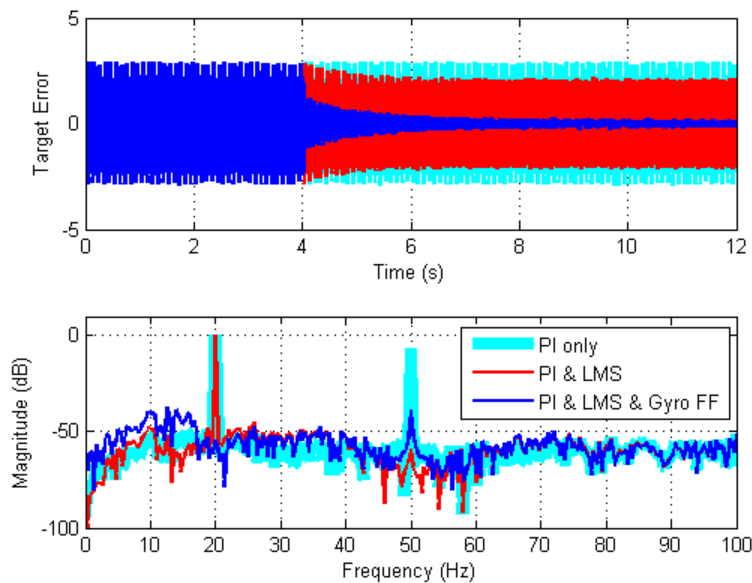


Figure 19. Jitter Control Simulation Results Using FX-LMS Algorithm

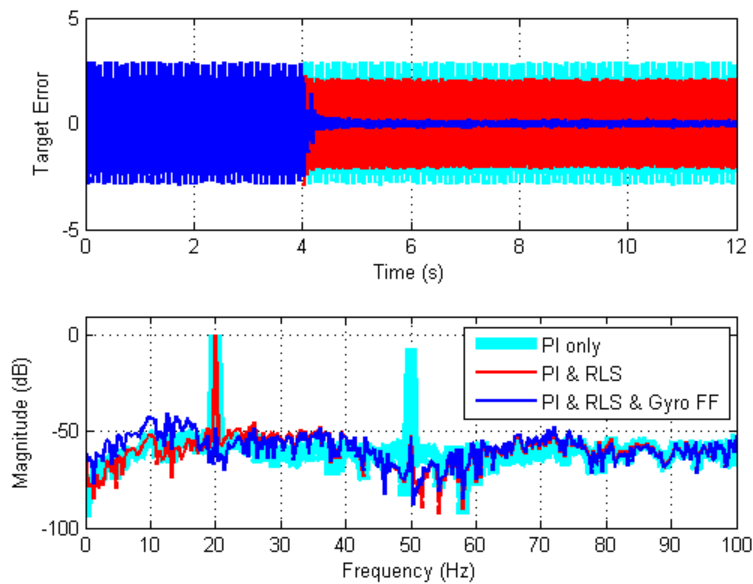


Figure 20. Jitter Control Simulation Results Using FX-RLS Algorithm

4. EXPERIMENTAL RESULTS

4.1 Narrow Field-of-View (NFOV) Video Tracker Control with Adaptive Filters

The NFOV video tracker control with adaptive filters verified in the computer simulation is implemented on the NFOV track loop of the testbed. FX-LMS experimental results are shown in Figures 21 and 22. In this case, the NFOV adaptive filter is active after approximately 35 seconds. With the sinusoidal target motion with a frequency of 0.5 Hz, NFOV track error was reduced by approximately 18 dB. FX-RLS experimental results are shown in Figures 23 and 24, and for this test the adaptive filter is active after approximately 35 seconds. NFOV error was reduced by approximately 19 dB at the 0.5 Hz disturbance frequency when using the FX-RLS algorithm.

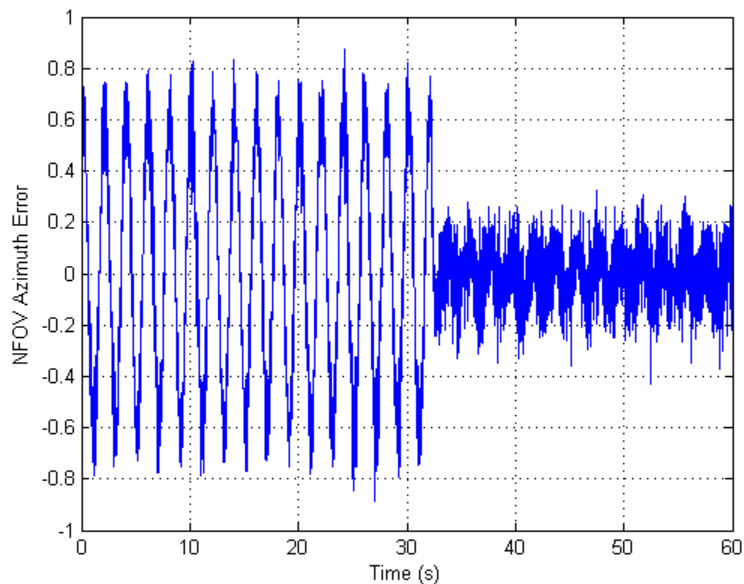


Figure 21. NFOV Track Error, FX-LMS algorithm

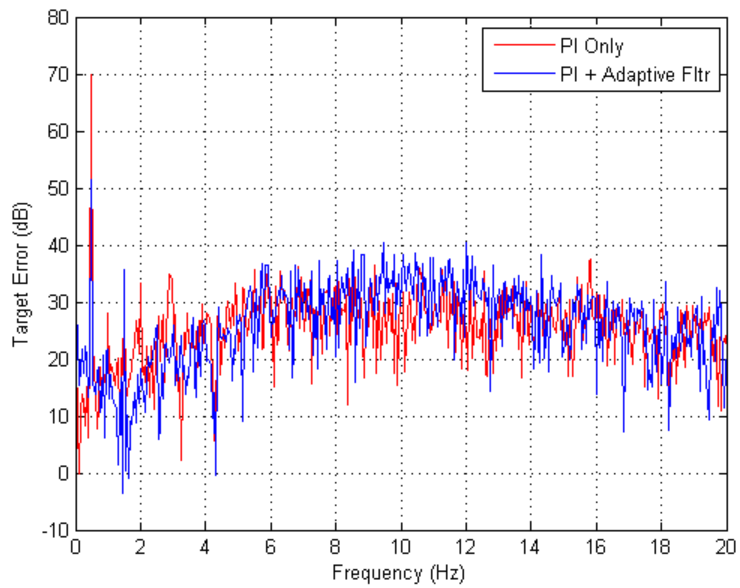


Figure 22. Frequency Domain NFOV track error, FX-LMS algorithm

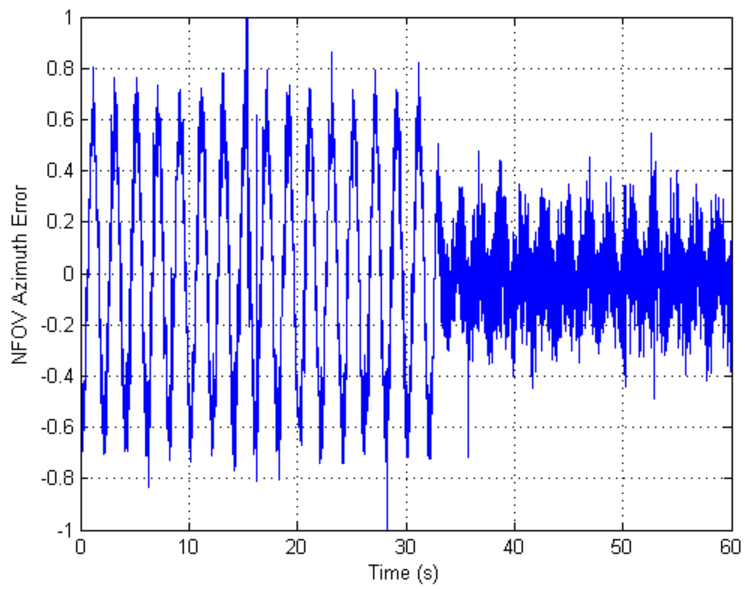


Figure 23. NFOV Track Error, FX-RLS algorithm

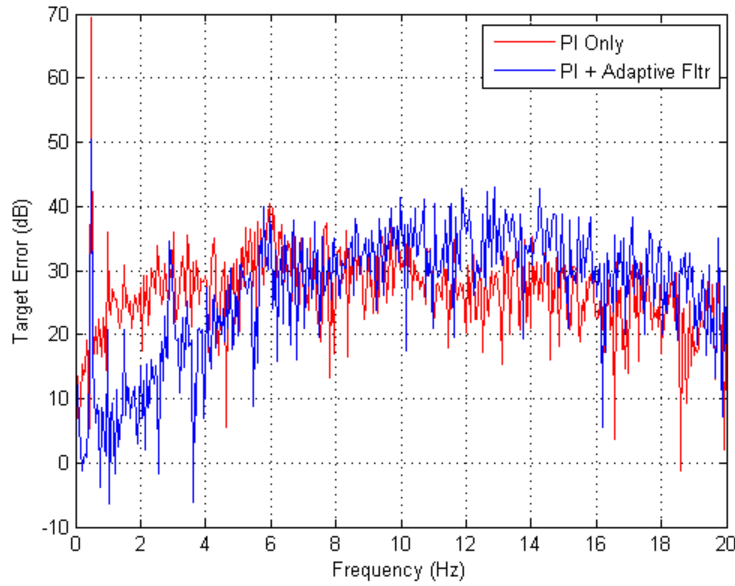


Figure 24. Frequency Domain NFOV track error, FX-RLS algorithm

4.2 Beam Jitter Control

Since additional rate gyros for strap-down type IRU implementation was not available at the time, a demonstration was conducted using the gimbal rate gyro. This gyro signal is applied as a feedforward control without adaptive filters implemented on the testbed. To accomplish feedforward control, the transfer function between the gyro and the FSM is required. This transfer function was developed using two tests, the first to determine the transfer function between the error at the PSD and the gyro and the second a transfer function between the FSM and the error at the PSD. Disturbance motion in both tests was detected by the PSD. This transfer function is summarized in equations 14 through 17 where y_{psd} is the error measured at the PSD, G_g is the transfer function between the gyro and the PSD, g is the gyro signal, G_{FSM} is the transfer function between the FSM and PSD and u is the control signal to the FSM. The FSM is modeled as a second order LPF. A system identification was conducted to determine G_g , which is a first order transfer function.

$$y_{psd} = G_g g \quad (14)$$

$$y_{psd} = -G_{FSM} u \quad (15)$$

$$u = -\frac{G_g}{G_{FSM}} g \quad (16)$$

$$G_g = \frac{1}{s + \tau}; \quad \tau = 1.6 \quad (17)$$

Since this was only a demonstration of the feasibility of strap-down type IRU implementation, the disturbance was limited to 5 Hz. The gains for both G_g and G_{FSM} were optimized for 5 Hz.

Experimental results for the gyro feedforward controller can be seen in Figures 25 and 26. The 5 Hz disturbance was turned on just prior to 3 seconds, and the feedforward controller was turned on after 6 seconds. It should be noted there was a boresight error, which caused the target error to be non-zero prior to application of the disturbance. By using the

gyro feedforward controller, target error at the disturbance frequency of 5 Hz was reduced by approximately 8 dB. Calibration of the system could produce further error reductions but was not attempted since these experiments were meant to simply demonstrate the feasibility of use the gyro signal in a feedforward controller.

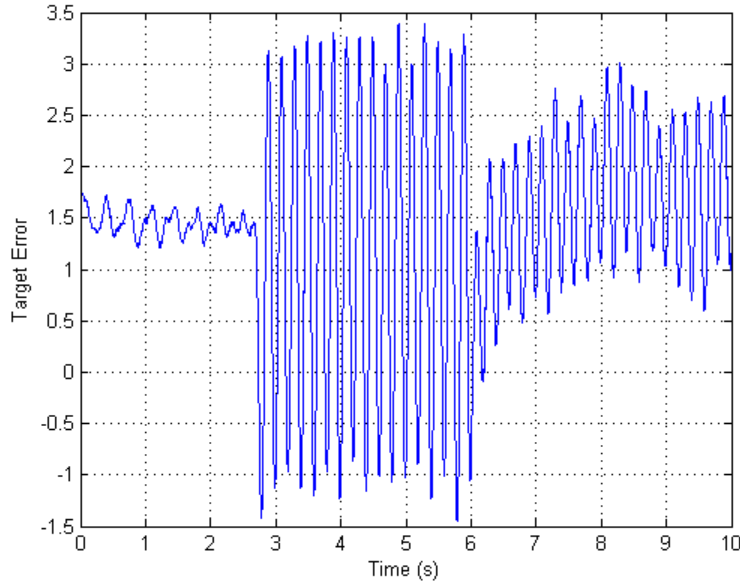


Figure 25. Frequency Domain NFOV track error, FX-RLS algorithm

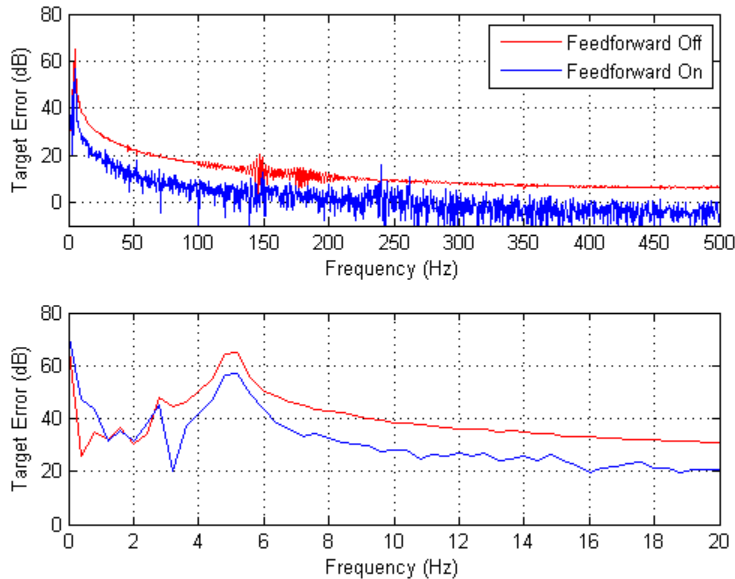


Figure 26. Frequency Domain NFOV track error, FX-RLS algorithm

5. CONCLUSIONS AND FUTURE WORK

In their research, a basic system characterization of the HEL testbed is performed prior to implementation of improved control design. This characterization resulted in the development of Matlab Simulink models, which proved useful in developing and testing new control methods. Adaptive filters using the FX-LMS and FX-RLS algorithms were simulated for the NFOV video tracker. Additionally, simulations were conducted using an strap-down type IRU for

adaptive controllers with multiple reference inputs. This controller contained a feedback adaptive filter using a signal from the PSD and a feedforward adaptive filter using a signal from the gyros. Both FX-LMS and FX-RLS algorithms were implemented on the NFOV video track loop of the HEL testbed. Experiments results show significant reduction in track error, especially at the target motion frequency. As a prelude to implementation of the strap-down type IRU adaptive controller, a simple gyro feedforward controller was implemented on the elevation axis of the HEL testbed. The experimental results showed improved beam pointing performance with a simple feedforward control. Additional work is required to complete implementing the control design for the strap-down type IRU. There are various possibilities in the jitter control system configuration with the strap-down type IRU, and the further work will be required to evaluate and demonstrate their performances.

ACKNOWLEDGEMENT

While not directly related to, the work presented here drew on much of the work in beam jitter control accomplished previously at NPS by Dr. Joseph Watkins, Brett Bateman, Michael Beerer and Dr. Hyungjoon Yoon [5], [7], [9].

REFERENCES

- [1] P. Orzechowski, N. Chen, S. Gibson, and T.-C. Tsao, "Adaptive Control of Jitter in a Laser Beam Pointing System," in Proceedings of the American Control Conference, Minneapolis, MN, USA, June 2006, pp. 2700-2705.
- [2] S. M. Kuo and D. R. Morgan, "Active Noise Control: A Tutorial Review," Proceedings of the IEEE, vol. 87, no. 6, pp. 943-973, Jun. 1999.
- [3] D. Kim, D. Frist, J. J. Kim, and B. Agrawal, "A HEL Testbed for High Accuracy Beam Pointing and Control," Naval Postgraduate School, Monterey, CA, Technical Report, 2009.
- [4] S. M. Kuo and D. R. Morgan, Active Noise Control Systems: Algorithms and DSP Implementations. New York: Wiley-Interscience, 1996.
- [5] M. Beerer, "Adaptive Filter Techniques for Optical Beam Jitter Control and Target Tracking," Masters thesis, Naval Postgraduate School, Monterey, CA, 2008.
- [6] S. Haykin, Adaptive Filter Theory, 4th ed. Upper Saddle River, New Jersey: Prentice Hall, 2002.
- [7] R. J. Watkin, "The adaptive control of optical beam jitter," Ph.D. dissertation, Naval Postgraduate School, Monterey, CA, Dec. 2004.
- [8] R. J. Watkins and B. N. Agrawal, "Use of least means squares filter in control of optical beam jitter," Journal of Guidance, Control and Dynamics, vol. 30, no. 4, pp. 1116-1122, Jul. 2007.
- [9] B. E. Bateman, "Experiments on laser beam jitter control with applications to a shipboard free electron laser," Master's thesis, Naval Postgraduate School, Monterey, CA, December 2007.